AEROELASTIC DYNAMIC STALL COMPUTATIONS OF A DOUBLE-SWEPT BLADE IN A FOUR-BLADED ROTOR CONFIGURATION

Georg Babij
Institute of Aeroelasticity, German Aerospace Center (DLR)
Bunsenstraße 10, 37073 Göttingen, Germany
georg.babij@dlr.de

Abstract

Innovative helicopter rotor blades with a combined forward-backward double-sweep at the outer part of the blade enable a reduction in noise emission and enhance the overall performance of a rotor. In this context, the influence of the aeroelastic behaviour in connection with the dynamic stall phenomenon is of great importance. It is accompanied by large aerodynamic load peaks, primarily seen in the lift and the pitching moment, impacting the structural integrity of the blades and adjacent control components. Double-swept model rotor blades were developed and investigated experimentally at the DLR Goettingen regarding the dynamic stall behaviour in a four-bladed rotor configuration at the Rotor Test Facility Goettingen. Due to an axial inflow to the rotor disc a sinusoidal variation in pitch angle is introduced to trigger the dynamic stall behaviour once per revolution. The experimental investigations were accompanied by aeroelastic as well as purely aerodynamic numerical simulations which are the main focus in this study. In case of the aeroelastic simulations, a tight coupling scheme was implemented to perform the data exchange between the inhouse CFD solver TAU and the commercial software Simpack as solver for multibody systems with flexible bodies in each time step. Six test cases with a rotational frequency of 23.6 Hz are presented comprising three with solely collective pitch angle and three with a superposed cyclic variation in pitch angle in order to introduce and strengthen the dynamic stall behaviour stepwise for the investigated rotor configuration. As a result, differences arise in the aerodynamic loads between both blade modelling approaches. They are elaborated in order to draw conclusions about the dynamic stall behaviour under consideration of elasticity in the blade modelling.

Keywords: Dynamic Stall, Flexible Multibody System, Computational Fluid Dynamics, Rotor Aeroelasticity

1 INTRODUCTION

Novel helicopter rotor blades with a combined forward-backward sweep at the outer part of the blade enable a reduction in noise emission and enhance the overall performance of a rotor [1]. In this context, the influence of the aeroelastic behaviour in connection with the dynamic stall phenomenon is of great importance. It is accompanied by large aerodynamic load peaks, primarily seen in the lift and the pitching moment, impacting the structural integrity of the blades and adjacent control components. Within the framework of the projects FAST– and URBAN–Rescue at the DLR, double-swept model rotor blades were developed [2] and investigated experimentally in a four-bladed rotor configuration at the Rotor Test Facility Goettingen (RTG) [3] which is shown in Figure 1. They are built from multiple layers of carbon fibre reinforced polymer with an integrated foam core and measure 541 mm in blade length as well as 72 mm in chord length at the root. The rotor radius amounts to 652 mm. Due to an axial inflow to the rotor a sinusoidal variation in pitch angle Θ is introduced to trigger the dynamic stall behaviour once per revolution. The following numerical study simulates the conducted experiments utilizing two different modelling approaches: on the one hand, an approach that incorporates aeroelasticity connected with elastic rotor blades, and on the other hand, one that considers the blades merely as rigid bodies. The corresponding computations are carried out with the use of computational fluid dynamics (CFD) and a multibody system (MBS) which is used in both cases, i.e. with

rigid and elastic modelled blades, to prescribe body motions. With the inclusion of aeroelasticity both domains are connected together by using a strong aeroelastic coupling scheme and, in addition, forces as well as displacements are exchanged between each other.

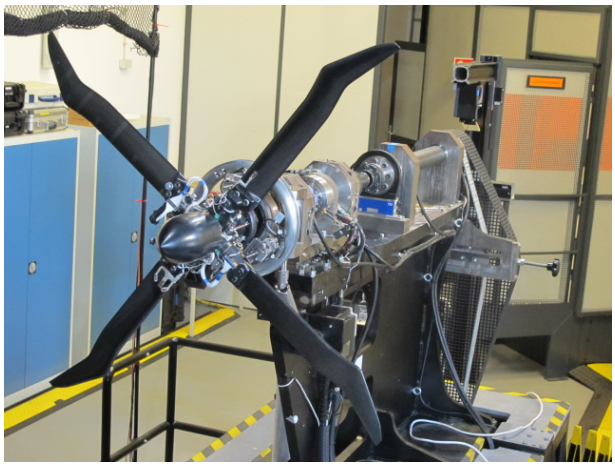

Fig. 1: Rotor Test Facility Göttingen with four-bladed rotor

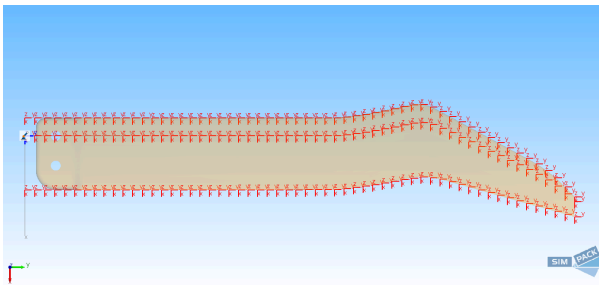

(a) Distribution of the markers on a blade

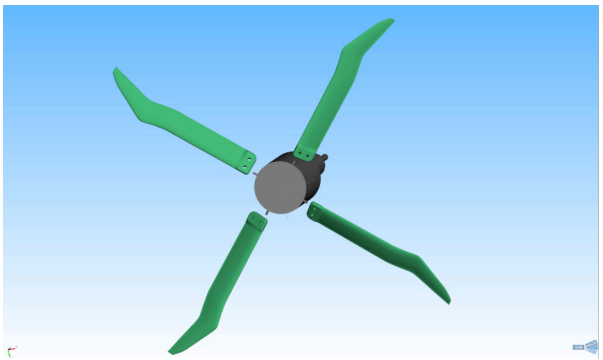

(b) Four-bladed rotor configuration

Fig. 2: Modelling of structural dynamics in Simpack (MBS)

2 NUMERICAL MODELLING

2.1 Structural dynamics

Simpack is used to describe the structural dynamics of the entire rotor by means of a multibody system. For the approach with flexible blades, the extension module FlexModal allows taking account of their elasticity. The structural displacements are thereby described in a modal representation with an underlying linear elastic material behaviour. 23 modal degrees of freedom are considered compromising the first 20 natural eigenmodes of the blade up to a corresponding eigenfrequency of 3129.90 Hz and 3 further inertia relief modes (IRM) as interface modes. Stiffening effects occurring due to huge centrifugal forces are considered by a geometric stiffness matrix. The first 5 eigenfrequencies in clamped boundary condition with their corresponding mode characterization can be found in Table 1 for the non-rotating system, i.e. $\Omega = 0$ Hz, and the considered operating point with $\Omega = 23.6$ Hz.

174 markers lying on 58 spanwise equidistantly distributed aerofoil cut sections with 3 markers per section serve on one hand as input for aerodynamic forces and on the other hand as output for structural displacements [4]. They are placed at the leading and trailing edge as well as at quarter chord position. Their distribution on one blade is shown in Figure 2a, whilst the entire MBS rotor configuration as modelled in Simpack is depicted in Figure 2b.

Mode No.	w.r.t. $\Omega = 0$ Hz	w.r.t $\Omega = 23.6$ Hz	Characterisation of the mode
1	43.81 Hz	51.30 Hz	1st flap
2	177.14 Hz	185.45 Hz	2nd flap
3	242.08 Hz	242.95 Hz	1st lag
4	316.26 Hz	319.91 Hz	1st torsion
5	455.85 Hz	461.27 Hz	3rd flap

Table 1: Eigenfrequencies of the clamped double-swept rotor blade and 0° pitch angle for rotor speed $\Omega = 0$ Hz [4] and $\Omega = 23.6$ Hz

2.2 Fluid dynamics

TAU utilizes the Reynolds-Averaged-Navier-Stokes (RANS) equations to model fluid flow [5]. Due to the unknown Reynolds stresses turbulence models are applied, such as the SST-k-ω-model according to Menter [6] in this study. Furthermore, a finite volume method implemented for unstructured grids is utilized to obtain a second-order accurate spatial discretization. Against this backdrop, an approximate solution is sought on a dual grid being computationally created from the user-defined primary grid. The primary grid contains approximately 13.555 million nodes and it consists of a background grid as well as four chimera grids representing the blades. A corresponding slice obtained by cutting through the middle of the domain is shown in Figure 3a. Figure 3b provides a zoom view of the primary grid nearby the blades. The time integration is performed by a

dual-time stepping approach with 500 iterations per physical time step Δt relying upon a two-step backward differentiation formula. Taking into account grid motion and deformation, the Chimera technique as well as the geometric conservation law were exploited.

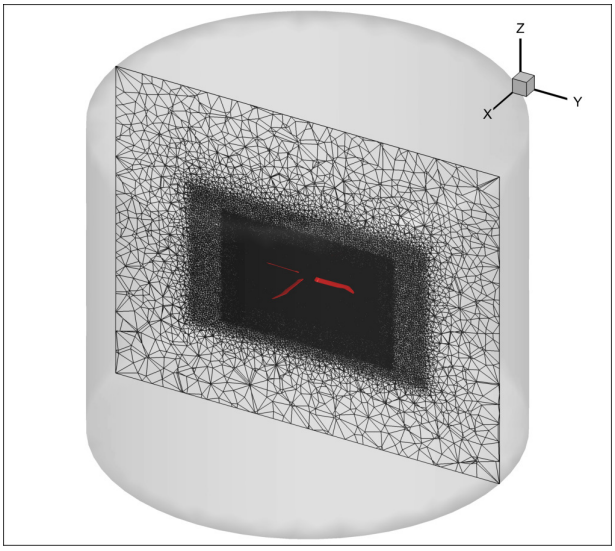

(a) Primary grid for the fluid domain

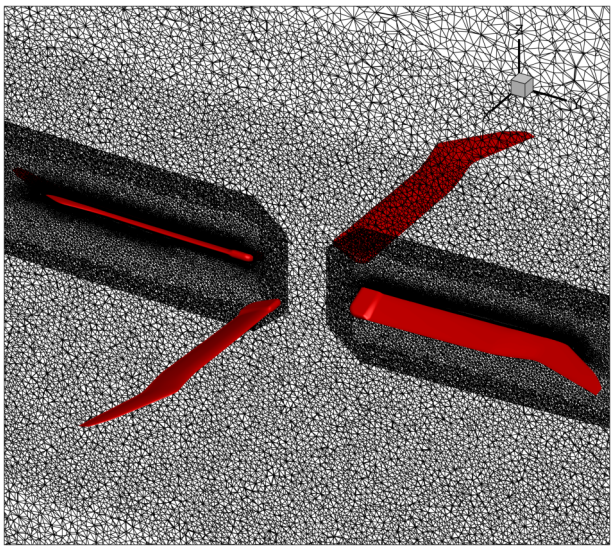

(b) Primary grid nearby the rotor blades

Fig. 3: Modelling of fluid dynamics in TAU (CFD)

2.3 Strong aeroelastic coupling scheme

The aeroelastic coupling is based on a sequential exchange of forces and displacements in each physical time step Δt between both solvers [7]. It represents in the sense of the terminology used within the rotorcraft community a strong coupling scheme. In detail, aerodynamic forces being calculated by TAU are transferred to Simpack and, vice versa, structural displacements together with rigid body motions are transferred from Simpack back to TAU. In order to exchange this data between both differently discretized domains, i.e. forces and displacements, scattered data interpolation methods based on radial basis functions are exploited. The individual steps that are run through in loop during one physical time step are described below [7, 8]:

1. Time integration in TAU either on the initial, undeformed grid or on a previously deformed grid
2. Extraction of the aerodynamic forces for all nodes on the blade surfaces
3. Transfer of the aerodynamic forces to the elastic MBS substructures by applying a scattered data interpolation based on radial basis functions (RBF) due to a different discretization of the CFD surface grids and the elastic MBS substructures
4. Time integration in Simpack with respect to the calculated aerodynamic forces
5. Extraction of the displacements as well as rigid body motions of the elastic MBS substructures
6. Transfer of the structural displacements onto the CFD surface grid nodes using RBF interpolation methods
7. Deformation of the chimera volume grids based on displacement of the blade surfaces
8. Applying the extracted rigid body motions onto the chimera blade grids .

In this study the physical time step is chosen according to an azimuthal discretization $\Delta\Psi = 1^\circ$, which results in approximately $\Delta t \approx 1.177 \cdot 10^{-4}$ s for a rotational frequency of $\Omega = 23.6$ Hz. The software implementation mostly relies upon DLR's framework FlowSimulator, which provides a powerful Python interface for tasks used in a CFD toolchain, e.g. controlling CFD simulations, data as well as grid im- and export, grid manipulation and interpolation [9].

3 NUMERICAL INVESTIGATIONS

Six test cases (TC) with a rotational frequency $\Omega = 23.6$ Hz will be presented comprising operating conditions with a solely collective pitch angle $\Theta_{coll} \in \{17^\circ, 24^\circ, 27^\circ\}$ and an additionally superposed cyclic variation in pitch angle $\Theta_{cyc} \in \{6^\circ, 8^\circ\}$. They serve to induce the dynamic stall phenomenon gradually with increasing strength. Their collective as well as cyclic pitch angle is given in Table 2 together with their predominant flow characteristics at the blades. All test cases are performed for two different modelling approaches: One that incorporates aeroelasticity connected with flexible rotor blades as well as one that considers the blades as rigid bodies. As

a result, the differences between both approaches are elaborated in order to draw conclusions about the dynamic stall behaviour under consideration of aeroelasticity. For this purpose, the total force F_n acting normal to the planform of a blade and the pitch moment M_y relative to an axis passing through the quarter chord point $(x = \frac{c}{4})$ at the blade root are monitored. Furthermore, the displacements at the blade tips are additionally extracted for computations including blade elasticity.

Similar to purely aerodynamic numerical studies in which blade elasticity is neglected, cf. Kaufmann et al. [10] and Letzgus et al. [11, 12], each test case is performed in such a manner that transients have subsided and a steady state has been reached for evaluation. Therefore, a vortex system is established in the computational domain with at least 10 and up to 20 simulated rotor revolutions that continuously exits at its boundaries.

TC No.	Θ_{coll}	Θ_{cyc}	predominant characteristics of fluid flow
1	17°	±0°	mostly attached flow conditions
2	24°	±0°	mostly attached flow conditions
3	27°	±0°	stall conditions
4	17°	±8°	mostly attached flow conditions for rigid blade modelling / onset of dynamic stall for elastic blade modelling
5	24°	±6°	light dynamic stall
6	27°	±6°	severe dynamic stall

Table 2: Overview of the investigated test cases (TC)

3.1 Computations with purely collective pitch angle Θ_{coll}

In the following section, three test cases with solely collective pitch angle will be presented whose results are summarized in Table 3.

TC No.	1	2	3
Θ_{coll} [°]	17°	24°	27°
F_n rigid [N]	29.5	61.5	72.0
F_n elastic [N]	29.1	60.7	71.5
M_y rigid [Nm]	-0.283	-0.631	-0.823
M_y elastic [Nm]	-0.302	-0.731	-0.834
w_n elastic [mm]	12.8	18.4	20.6

Table 3: Results for test cases with purely collective pitch angle

3.1.1 Test case 1 with $\Theta_{coll} = 17°$ (attached flow conditions)

The collective pitch angle amounts $\Theta_{coll} = 17°$ for TC 1. Despite the occurrence of unsteady vortex shedding due to flow separation in the boundary layer at the root of the rotor blades, attached flow conditions at the blade surfaces as well as distinctive vortices trailing the tips are characteristic for this test case with both blade modelling approaches. Although no significant lift forces are induced at the root area, the vortex shedding leads to slight fluctuations in the total aerodynamic load on the blades. For an approach with rigid blades, all four blades experience a mean normal force $F_n \approx 29.5$ N and a mean pitch moment $M_y \approx -0.283$ Nm. When considering blade elasticity, the blade normal force on one blade decreases to $F_n \approx 29.1$ N which is due to a twisting of the blade in nose-down direction. The twist constantly increases in spanwise direction and reaches its maximum at the blade tip. Since the centre of pressure moves towards the trailing edge with increased twist towards nose-down direction, the magnitude of the pitch moment acting in nose-down direction is also increased. Therefore, it amounts $M_y \approx -0.302$ Nm for a elastic blade modelling and the displacement of the blade tip amounts $w_n \approx 12.8$ mm.

3.1.2 Test case 2 with $\Theta_{coll} = 24°$ (attached flow conditions)

In TC 2, the collective pitch angle is raised to $\Theta_{coll} = 24°$. Attached flow conditions at the blade surfaces as well as distinctive vortices at the blade tips are still the predominant characteristics for both blade modelling approaches. The vortex shedding occurring in the region of the blade roots is enlarged compared to TC 1. For an approach with rigid blade modelling, each of the four blades experiences a mean normal force $F_n \approx 61.5$ N and a mean pitch moment $M_y \approx -0.631$ Nm, whereby the values fluctuate over time due to the aforementioned unsteady flow separation at the blade roots. In contrast to this, an approach with elastic blade modelling shows lower mean blade normal forces $F_n \approx 60.7$ N and a mean pitch moments $M_y \approx -0.731$ Nm. As described in TC 1, the change in blade twist leads to a decrease of the blade normal force and an increase in the magnitude of pitch moment acting towards nose-down direction. The blade tips bend up with a normal deflection $w_n \approx 18.4$ mm. As an illustration of the bending behaviour regarding shape and strength, one deformed double-swept blade is shown in comparison to its undeformed state in Figure 4. Furthermore, insight into the flow field is given in Figure 5 where the vortex system is illustrated by means of the λ_2-criterion.

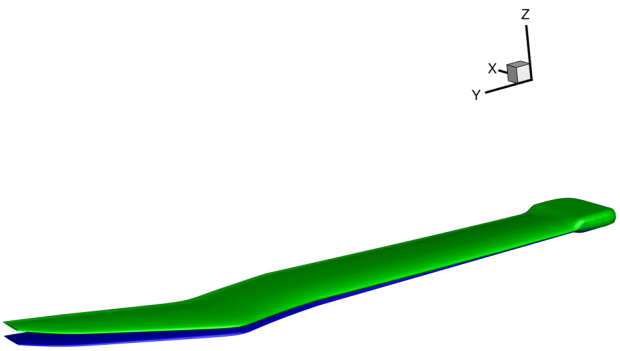

Fig. 4: Blade deformation for TC 2 (Θ = 24° ± 0°) deformed (green) versus undeformed (blue) blade

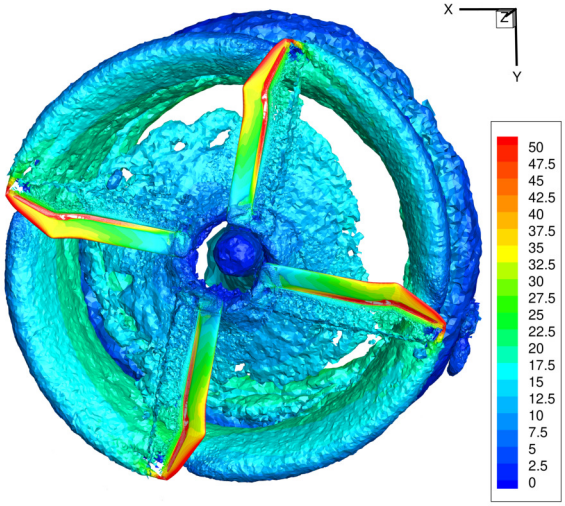

Fig. 5: Vortex system with flexible blades for TC 2 with Θ = 24°±0°
(illustrated with λ_2-criterion and coloured by magnitude of flow velocity [$\frac{m}{s}$])

3.1.3 Test case 3 with $\Theta_{coll} = 27°$ (stall conditions)

In TC 3, the collective pitch angle is raised a second time so that now additional vortex shedding due to flow separation can be observed on the backward swept part of the rotor blade in contrast to TC 1 and 2. These shed vortices immediately interact with the trailing vortex at the blade tip and unite to form a larger vortex. Furthermore, there are still vortices shed at the blade roots, analogous to TC 1 and 2. For these reasons, TC 3 is characterized by stall conditions. Due to the strong flow separation, the values for the aerodynamic loads also fluctuate strongly. For an approach with rigid blade modelling, each of the four blades experiences a mean normal force $F_n \approx 72.0$ N and a mean pitch moment $M_y \approx -0.823$ Nm. Due to the aforementioned change in twist with the consideration of blade elasticity, the normal force on one blade decreases to $F_n \approx 71.5$ N and the pitch moment changes to $M_y \approx -0.834$ Nm. However, the differences in the aerodynamic loads between both modelling approaches are not as large as in TC 2 which can be attributed to the present flow separation on the backward swept part of the rotor blade. As a result, the centre of pressure only moves slightly to the trailing edge, so that there is also only a slight change in the pitch moment. The displacement of the blade tip amount for this test case $w_n \approx 20.6$ mm.

3.2 Computations with superposed cyclic pitch angle Θ_{cyc}

3.2.1 Test case 4 with $\Theta = 17° \pm 8°$ (rigid: attached flow conditions / elastic: onset of dynamic stall)

Starting from TC 1, an additional cyclic pitch angle is imposed which results in a setup with a pitch angle variation Θ = 17° ± 8°. Analogous to TC 1, the occurrence of unsteady vortex shedding due to flow separation can be observed at the blade roots as well as distinctive vortices at the blade tips. On the blade surfaces the fluid flow stays mostly attached for a rigid blade modelling whereby for an elastic modelling approach flow separation also occurs on the upper blade surface in regions near the outer kink in the vicinity of maximum pitch angle.

This different behaviour between both blade modelling approaches is also reflected in the aerodynamic loads F_n and M_y by plotting the periodic values of one revolution against pitch angle Θ, shown in Figure 6a and 6b for an elastic as well as rigid blade modelling. A hysteresis behaviour becomes apparent which is characterised by different values for the up- and downstroke and caused by non-linearities, e.g. flow separation on the blade surfaces. When looking at the blade normal force F_n and pitch angles in the vicinity of the maximum value $20° < \Theta < 25°$, the curves for up- and downstroke differ from each other for an elastic modelling approach due to the occurring flow separation on the outer kink of the blade. A vortex is formed at the flow separation point holding his position and not being shed even for most of the time during the downstroke. Therefore, the values in the blade normal force are higher during the downstroke than the upstroke. In case of a rigid blade modelling, both curves stay close together in this region and flow separation is not evident. Most apparent are the differences between both blade modelling approaches in the curves of the pitch moment M_y. Although the normal blade force F_n stays for both modelling

approaches in the same range of minimum and maximum value, the magnitude of the pitch moment M_y is larger for high pitch angles Θ in the case of an elastic blade modelling approach. Due to negative values, the pitch moment acts in nose-down direction on the blade. Excited by the aerodynamic loads the rotor blades primarily perform a bending vibration which is captured by the blade tip displacement. Moreover, the blade tip displacement also shows a non-linear behaviour where up- and downstroke differ from each other, shown in Figure 6c. The maximum value in blade tip displacement is reached during the first part of downstroke indicating that vorticity is still produced at this stage feeding larger vortices on the upper blade surface.

By casting the values of the normal blade force F_n as well as the normal blade displacement w_n from time into frequency domain the influence of higher rotor harmonics becomes clear, shown in Figure 7a and 7b. The rotor harmonics of the blade normal force $\hat{F}_n$ show beside a dominant first rotor harmonic at $f_1 = 23.6$ Hz also a small participation of the second one at $f_2 = 47.2$ Hz and third one at $f_3 = 70.8$ Hz. A comparison between both blade modelling approaches reveals slightly higher amplitudes for the first two rotor harmonics f_1 and f_2 in case of a rigid modelling. This is caused by a reduced aerodynamic angle of attack related to the almost in phase blade bending behaviour of the rotor blades beside blade twist in nose-down direction. This means that the phase shift between blade tip displacement and the blade normal force is neglectable due to the high stiffness of the rotor blades. Analogous to the normal blade force, the motion of the blade tip displacement also mainly consists of the first two rotor harmonics f_1 and f_2 whereby the second rotor harmonic lies in the vicinity of the first bending eigenfrequency which amounts $f_{bend} = 50.43$ Hz for a constant collective pitch angle $\Theta_{coll} = 17°$. It slightly decreases for higher pitch angles, cf. Table 1 for $\Theta_{coll} = 0°$. Against this background, it can easily be excited by even small amplitudes.

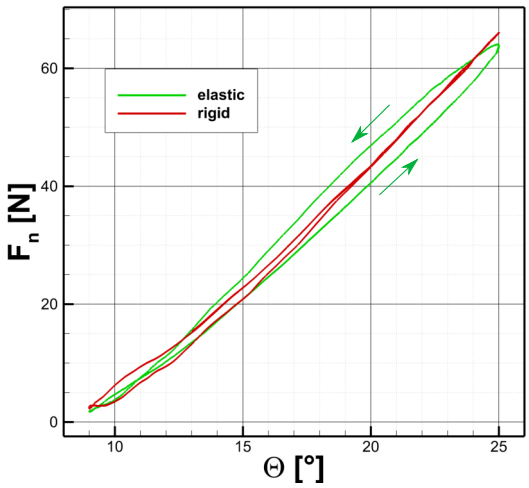

(a) Normal force $F_n(\Theta)$
elastic and rigid blade modelling
(course of time only indicated for elastic modelling ↑)

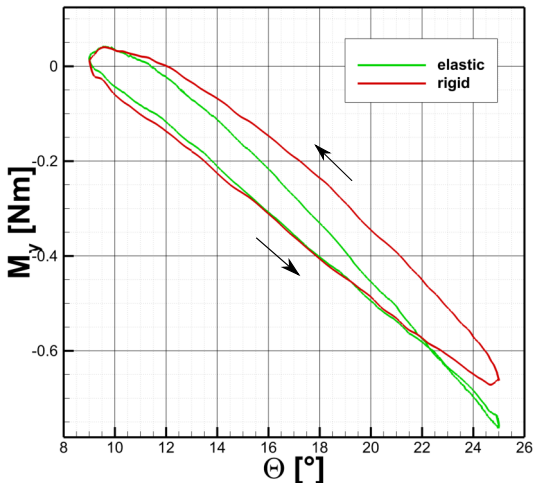

(b) Pitch moment $M_y(\Theta)$
elastic and rigid blade modelling

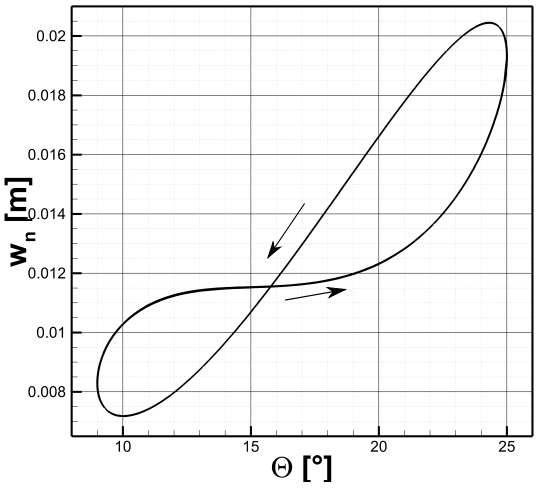

(c) Blade tip displacement $w_n(\Theta)$

Fig. 6: Aerodynamic loads and normal displacement at the blade tip during one revolution with superposed cyclic pitch Θ = 17°±8°
(course of time is indicated with adjacent arrows ↑)

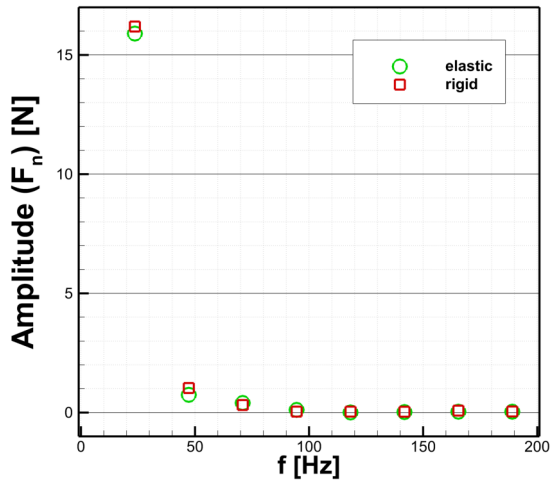

(a) Normal blade force $\hat{F_n}(f)$
elastic and rigid blade modelling

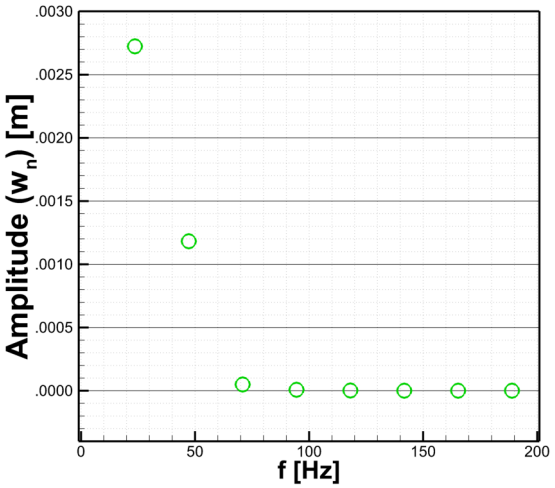

(b) Blade tip displacement $\hat{w_n}(f)$
elastic blade modelling

Fig. 7: Rotor harmonics for Θ = 17°±8° (TC 4)

3.2.2 Test case 5 with $\Theta = 24° \pm 6°$ (light dynamic stall)

Starting from TC 2 with $\Theta_{coll} = 24°$, an additional cyclic pitch angle of $\Theta_{cyc} = 6°$ is superposed which now induces a light dynamic stall behaviour at the rotor blades for both blade modelling approaches. The fluid flow separates from the upper blade surface in regions near the outer kink as well as at the backward-swept part in close vicinity to the blade tip. As a consequence, additional vortices are shed into the flow field beside those trailing the blades at its tips and non-linearities are increased compared to TC 4. In the case of a rigid blade modelling the course of the curve for the normal blade force F_n now clearly differs during up- and downstroke which indicates the beginning of a collapse of the blade normal force at maximum pitch angle, see Figure 8a. In contrast to this, the curves for up- and downstroke lie close together in the case of an elastic blade modelling. Furthermore, an intersection point is recognisable between the up- and downstroke as in TC 4 whereby it now lies in upper right section of the hysteresis loop. By casting the time signal into frequency domain the rotor harmonics mainly show a significant participation of a dominant first one at $f_1 = 23.6$ Hz and second one at $f_2 = 47.2$ Hz, see Figure 9a, whereby differences between both blade modelling approaches are also observed. Under consideration of elasticity the first rotor harmonic is slightly increased in contrast to the second one which is minimally weakened.

Analogous to TC 4, the magnitude of the pitch moment M_y is greater in the case of an elastic blade modelling, see Figure 8b. Moreover, the differences between a rigid and elastic blade modelling increase so that in the vicinity of the maximum pitch angle both curves differ by up to 0.19 Nm. Moreover, the pitch moment now starts to collapse in the vicinity of maximum pitch angle. It is a result of moving vortices over the aerofoil previously being induced by flow separation and shed at the trailing edge afterwards.

When looking at the blade tip displacement, a predominant participation of the first and second rotor harmonic can be found as shown in Figure 9b. As already mentioned for TC 4, the second rotor harmonic lies in the vicinity of the first bending eigenfrequency which is therefore easily made to resonate. In the time domain, this behaviour is depicted as a hysteresis loop shown in Figure 8c in which up- and downstroke differ from each other. In contrast to TC 4 (cf. Figure 6c), the blade tip displacement now reaches its maximum value already at the end of the upstroke.

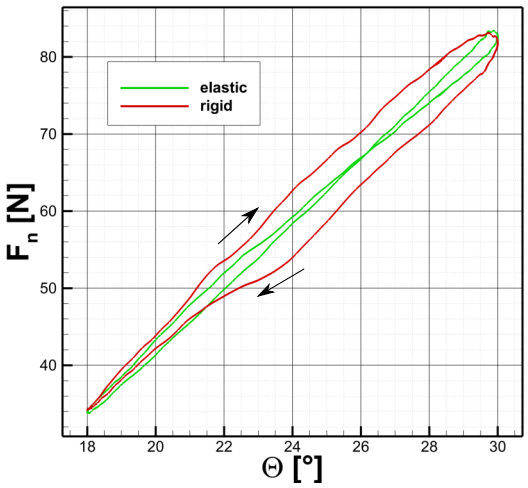

(a) Normal force $F_n(\Theta)$
rigid and elastic blade modelling

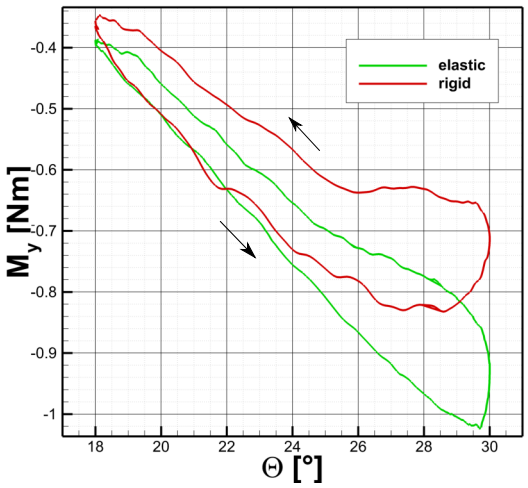

(b) Pitch moment $M_y(\Theta)$
rigid and elastic blade modelling

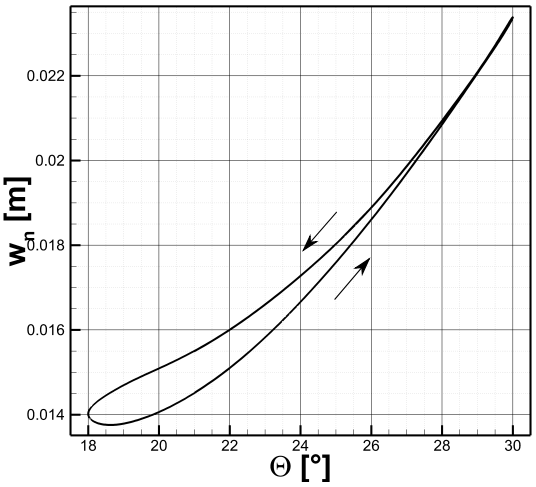

(c) Blade tip displacement $w_n(\Theta)$

Fig. 8: Aerodynamic loads and normal displacement at the blade tip during one revolution with superposed cyclic pitch Θ = 24°±6° (course of time is indicated with adjacent arrows ↑)

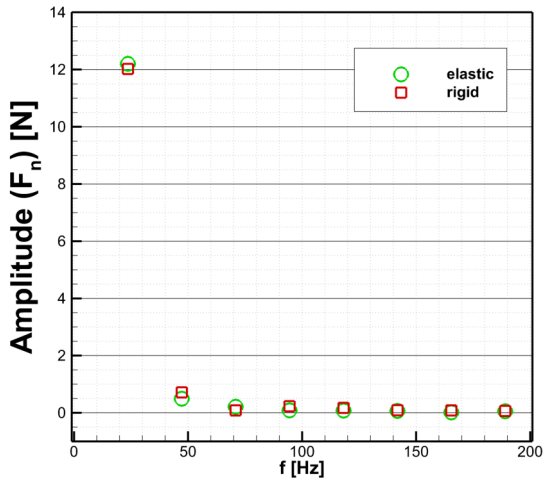

(a) Normal blade force $\hat{F}_n(f)$
rigid and elastic blade modelling

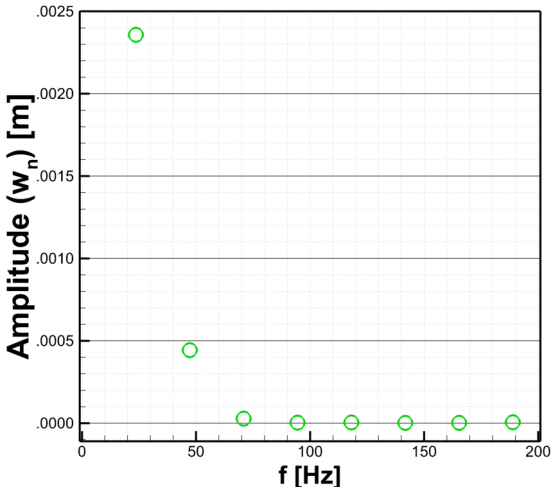

(b) Blade tip displacement $\hat{w}_n$
elastic blade modelling

Fig. 9: Rotor harmonics for Θ = 24°±6° (TC 5)

3.2.3 Test case 6 with $\Theta = 27° \pm 6°$ (severe dynamic stall)

In order to strengthen the dynamic stall behaviour, the collective pitch angle is further increased to $\Theta_{coll} = 27°$, cf. TC 3 in which stall conditions are already present for the constant collective part of pitch angle. This results in a setup with a pitch variation of $\Theta = 27° \pm 6°$. Large vortex structures are shed during the upstroke, even on the forward swept part of the blade. The occurrence of distinctive vortices originating from blade tips remains, however they are clearly weakened as the vorticity is already shed off by flow separation. Therefore, TC 6 is characterized by severe dynamic stall behaviour.

In contrast to TC 4 and 5, the curves for the normal blade force F_n deviate strongly from each other during up- and downstroke for both blade modelling approaches, see Figure 10a. Therefore, rigid and elastic blade modelling show a collapse in the vicinity of maximum pitch angle which is larger in case of rigid blade modelling. It amounts approximately 24 N for the rigid blade modelling compared to 19 N for the elastic blade modelling. Due to the fact that the hysteresis loop for rigid blade modelling almost envelops the one for an elastic modelling, the differences between up- and downstroke are greater in case of rigid blade modelling. Moreover, the frequency spectrum illustrates this fact in Figure 11a whereby the second rotor harmonic at $f_2 = 47.2$ Hz is higher in case of rigid blade modelling. The participation of a third one at $f_3 = 70.8$ Hz, fourth one at $f_4 = 94.4$ Hz and fifth one at $f_5 = 118.0$ Hz is primarily responsible for slight oscillations being observable during the downstroke.

Analogous to TC 4 and 5, the magnitude of the pitch moment M_y at high pitch angles is larger in case of elastic blade modelling, see Figure 10b. The difference to the maximal magnitude with rigid blade modelling approximately lies by 0.23 Nm. Both hysteresis loops are separated from each other whereby the magnitude values for rigid blade modelling are lower. Furthermore, the collapse in the pitch moment at high pitch angles is lower for the rigid blade modelling.

When looking at the blade tip displacement w_n, the frequency spectrum reveals compared to TC 4 and 5 an additional significant participation of the third rotor harmonic beside the first and second one, see Figure 11b. This circumstance is due to the occurrence of higher rotor harmonics in the aerodynamic loads with strengthened dynamic stall behaviour. In case of the normal blade force F_n, it includes rotor harmonics up to fifth order. The corresponding time signal also shows quite strikingly a upward motion of the blade tip during the downstroke where the rotor blade bends up again, see Figure 10c.

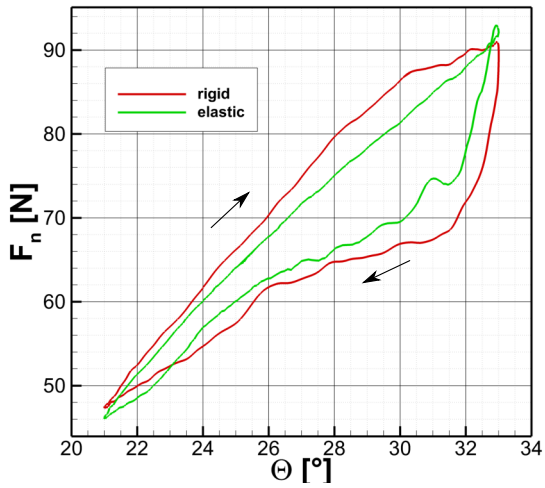

(a) Normal force $F_n(\Theta)$
rigid and elastic blade modelling

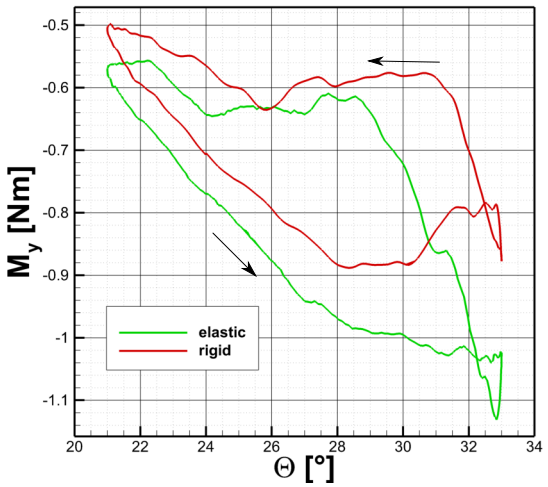

(b) Pitch moment $M_y(\Theta)$
rigid and elastic blade modelling

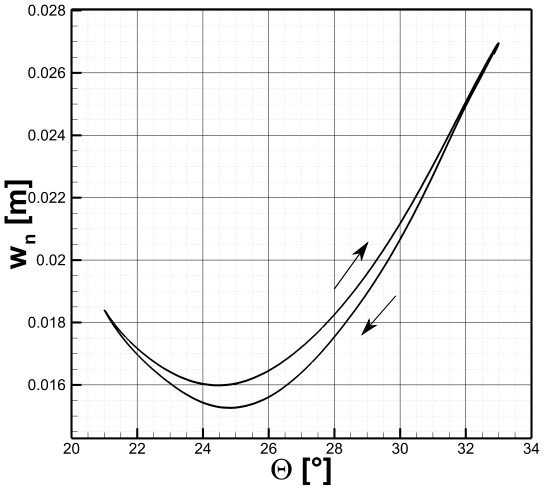

(c) Blade tip displacement $w_n(\Theta)$

Fig. 10: Aerodynamic loads of a blade and normal displacement at the blade tip during one revolution with superposed cyclic pitch Θ = 27°±6°
(course of time is indicated with adjacent arrows ↑)

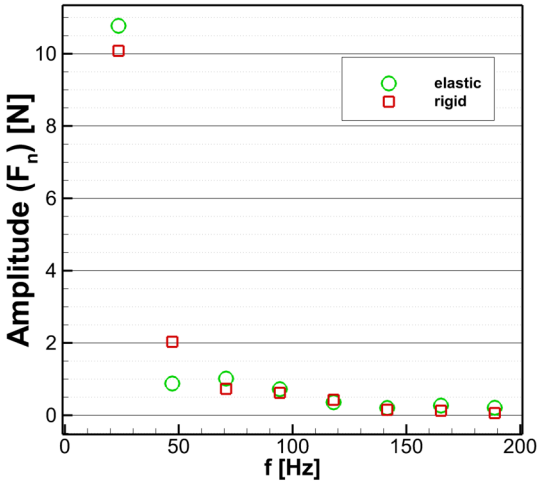

(a) Normal blade force $\hat{F_n}(f)$
rigid and elastic blade modelling

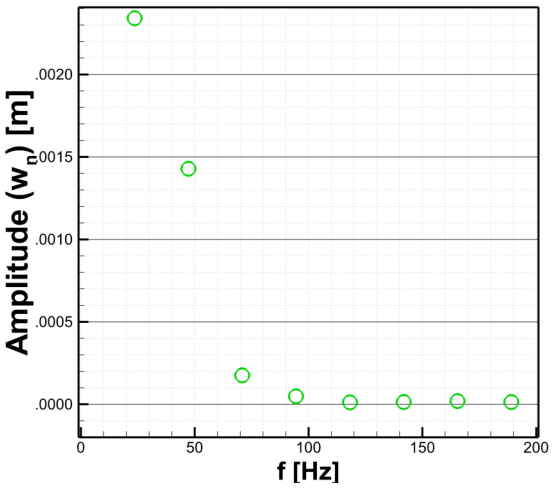

(b) Blade tip displacement $\hat{w_n}(f)$
elastic blade modelling

Fig. 11: Rotor harmonics for Θ = 27°±6° (TC 6)

4 SUMMARY AND CONCLUSION

Six test cases were investigated numerically for a four-bladed rotor configuration with double-swept rotor blades and a rotational frequency $\Omega = 23.6$ Hz. Three test cases comprise operating conditions with a solely collective pitch $\Theta_{coll} \in \{17°, 24°, 27°\}$. Following on from this, an additionally cyclic variation in pitch angle is superposed on the test cases with collective pitch angle. It results in sinusoidal pitch angle variations $\Theta \in \{17° \pm 8°, 24° \pm 6°, 27° \pm 6°\}$ and induce the dynamic stall phenomenon gradually with increasing strength. All test cases were simulated with rigid and elastic modelled rotor blades in order to elaborate the differences between both blade modelling approaches and draw conclusions about the dynamic stall behaviour under consideration of aeroelasticity.

Looking at test cases with solely collective pitch angle, the normal blade force F_n is slightly reduced whereby the magnitude of the pitch moment increases acting minimally more in nose-down direction. The decrease amounts to approximately 1 N for the blade normal force F_n and the increase in magnitude of the pitch angle is in all three test cases less or equal 0.1 Nm. The increased magnitude of the pitch moment generally leads to higher forces in the pitch link rods which have not been included in the Simpack model. The maximum blade tip displacement amounts to 20.6 mm for TC 3 with a collective pitch $\Theta_{coll} = 27°$.

For test cases with additional cyclic pitch angle, the hysteresis curves differ between a rigid and elastic blade modelling with strengthened dynamic stall behaviour. In general, it can be stated that the curves for up- and downstroke of the normal blade force F_n are further apart from each other in the test cases with dynamic stall (TC 4 & 5) and rigid blade modelling. Consequently, the collapse of the force is also larger for the rigid blade modelling. It amounts for the test case with severe dynamic stall (TC 6) to approximately 24 N compared to 19 N with elastic blade modelling. Furthermore, aerodynamic nonlinearities are growing with the onset and strength of the dynamic stall behaviour which leads to an increase of the second and higher rotor harmonics in the frequency spectrum. When comparing the rotor harmonics for both blade modelling approaches and test cases with dynamic stall (TC 5 & 6), it can be stated that the first rotor harmonic is increased whereas the second one is decreased when coming from a rigid to an elastic blade modelling approach. In the case of TC 4, the first and second rotor harmonic are both slightly reduced. The changes in the rotor harmonics are due to blade bending vibrations which are captured by the blade tip displacement. They are excited by normal forces acting on the blades and mainly include a participation of the first and second rotor harmonic in all test cases with cyclic pitch angle variation. However, for this specific rotor blade the second rotor harmonic is easily made to resonate, since it lies close to the first bending eigenfrequency of the blade. With growing strength of the dynamic stall behaviour the participation of additional rotor harmonics rises, for example the third rotor harmonic in TC 6. The magnitude of the pitch moment M_y increases with onset and growth of the dynamic stall behaviour while including blade elasticity. Furthermore, it acts stronger towards the nose-down direction and its hysteresis curve shifts towards more negative values, especially in the range of high pitch angles.

As a final conclusion, the inclusion of blade elasticity influences the aerodynamic blade loads whereby the differences between a rigid and elastic blade modelling are related to the strength of the dynamic stall behaviour. The forces acting on the pitch link rods are greater on consideration of blade elasticity due to higher peak values in the pitch moment of the blades. Therefore, the connected pitch link rods are more stressed.

5 OUTLOOK

As a next step, experimental data which include measured blade forces and moments as well as pressure data for the numerical investigated test cases are available for comparison. In order to simulate forward flight, further investigations will focus on a wind tunnel rotor configuration with an radial inflow from the front at 180° azimuth.

6 COPYRIGHT STATEMENT

7 REFERENCES

[1] W.R. Splettstößer, Berend G. van der Wall, B. Junker, K.-J. Schultz, P. Beaumier, Y. Delrieux, P. Leconte, and P. Crozier. The ERATO Programme: Wind Tunnel Results and Proof of Design for an Aeroacoustically Ouptimized Rotor. In *25th European Rotorcraft Forum*, September 1999.

[2] Martin Michael Müller, Till Schwermer, Holger Mai, and Christian Stieg. Development of an innovative double-swept rotor blade tip for the rotor test facility Goettingen. In *DLRK 2018 - Deutscher Luft- und Raumfahrtkongress*, September 2018.

[3] Till Schwermer, Kai Richter, and Markus Raffel. Development of a Rotor Test Facility for the Investigation of Dynamic Stall, 2016.

[4] Jürgen Arnold and Stefan Waitz. Using Multibody Dynamics for the Stability Assessment of a New Double-Swept Rotor Blade Setup. Delft, 2018. European Rotorcraft Forum.

[5] D. Schwamborn, T. Gerhold, and R. Kessler. DLR-TAU Code - an Overview. In *1st ONERA/DLR Aerospace Symposium, Paris, 21.-24. Juni 1999*, pages S4–2–S4–10, 1999. LIDO-Berichtsjahr=1999,.

[6] F. R. Menter. Two-equation eddy-viscosity turbulence models for engineering applications. *AIAA Journal*, 32(8):1598–1605, 1994.

[7] Stefan Surrey, B. Ortun, K.-V. Truong, and Felix Wienke. Investigation of the structural blade dynamics and aeroelastic behavior of the 7A rotor. West Palm Beach, 2016. American Helicopter Society 72nd Annual Forum.

[8] Georg Babij. Aeroelastic dynamic stall computations of a double-swept rotor blade. In *20th STAB-Workshop*, November 2021.

[9] Michael Meinel and Gunnar O. Einarsson. The FlowSimulator framework for massively parallel CFD applications. In *PARA2010*, June 2010.

[10] Kurt Kaufmann, Martin M. Müller, and Anthony D. Gardner. Dynamic stall computations of double-swept rotor blades. In Andreas Dillmann, Gerd Heller, Ewald Krämer, Claus Wagner, Cameron Tropea, and Suad Jakirlić, editors, *New Results in Numerical and Experimental Fluid Mechanics XII*, pages 351–361, Cham, 2020. Springer International Publishing.

[11] Johannes Letzgus, Manuel Keßler, and Ewald Krämer. CFD-Simulation of three-dimesional dynamic stall on a rotor with cyclic pitch control. Delft, 2015. European Rotorcraft Forum.

[12] Johannes Letzgus, Anthony Gardner, Till Schwermer, Manuel Keßler, and Ewald Krämer. Numerical investigations of dynamic stall on a rotor with cyclic pitch control. *Journal of the American Helicopter Society*, 64:1–14, 01 2019.